Accepted Manuscript

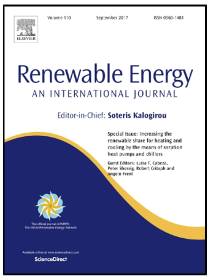

Analysis of electrical drive speed control limitations of a power take-off system for wave energy converters

José F. Gaspar, Mojtaba Kamarlouei, Ashank Sinha, Haitong Xu, Miguel Calvário, François-Xavier Faÿ, Eider Robles, C. Guedes Soares

PII:	S0960-1481(17)30479-2
DOI:	10.1016/j.renene.2017.05.085
Reference:	RENE 8852
To appear in:	*Renewable Energy*
Received Date:	30 December 2016
Revised Date:	19 May 2017
Accepted Date:	28 May 2017

Please cite this article as: José F. Gaspar, Mojtaba Kamarlouei, Ashank Sinha, Haitong Xu, Miguel Calvário, François-Xavier Faÿ, Eider Robles, C. Guedes Soares, Analysis of electrical drive speed control limitations of a power take-off system for wave energy converters, *Renewable Energy* (2017), doi: 10.1016/j.renene.2017.05.085

Analysis of electrical drive speed control limitations of a power take-off system for wave energy converters

José F. Gaspar[a], Mojtaba Kamarlouei[a], Ashank Sinha[a], Haitong Xu[a], Miguel Calvário[a], François-Xavier Faÿ[b], Eider Robles[b], C. Guedes Soares[a],*

[a] Centre for Marine Technology and Ocean Engineering (CENTEC), Instituto Superior Técnico, Universidade de Lisboa, Av. Rovisco Pais, 1049-001 Portugal.

[b] TECNALIA. Energy and Environment Division, Parque Tecnológico de Bizkaia, 48160 Derio, Spain.

*Corresponding author E-mail address: c.guedes.soares@centec.tecnico.ulisboa.pt

Abstract: The active control of wave energy converters with oil-hydraulic power take-off systems presents important demands on the electrical drives attached to their pumps, in particular on the required drive accelerations and rotational speeds. This work analyzes these demands on the drives and designs reliable control approaches for such drives by simulating a wave-to-wire model in a hardware in-the-loop simulation test rig. The model is based on a point absorber wave energy converter, being the wave, hydrodynamic and oil-hydraulic part simulated in a computer that sends and receives signals from the real embedded components, such as the drive generator, controller and back-to-back converter. Three different control strategies are developed and tested in this test rig and the results revealed that despite the drive limitations to acceleration levels, well above 1×10^4 rpm/s, these do not significantly affect the power take-off efficiency, because the required acceleration peaks rarely achieve these values. Moreover this drive is much more economical than an oil-hydraulic and equivalent one that is able to operate at those peaks of acceleration.

Keywords: Wave energy converter, Power take-off, Electrical drives, Hydraulic transformer, Wave-to-Wire Model.

1. Introduction

According to Falcão [1], Drew et al. [2] and Guedes Soares et al. [3], among others, high-pressure oil-hydraulic Power Take-Off (PTO) systems are suitable for slow oscillating body type wave energy converters (WEC) actuated by large wave forces [1, 4]. Moreover, this technology is suitable for reactive control of the WEC [5-9], an approach developed to extract maximum power from the wave by adjusting the WEC oscillatory movement in order to match its natural frequency with the wave frequency. On the other hand, hydrostatic drives can support accelerations far above the electrical drives. For example, the oil-hydraulic pump has a lower natural moment of inertia and, when operating in motor mode, higher dynamic response with speed variations up to 80000 rpm/s for a 100 kW machine than an equivalent electrical power drive running at 7500 rpm/s [10]. The power range supported by both technologies is also different, between 70 to 700 kW and 7 to 200 kW for hydrostatic secondary and electrical alternating current (AC) frequency controlled drives, respectively [10]. Moreover, the cooling effect provided by the oil itself is also an important advantage over the electrical drives [10].

So, the use of electrical drives depends on their localization in the power conversion chain. For example, Hansen et al. [11, 12] present a PTO system made up of two distinct oil-hydraulic systems, as presented in Figure 1. The first is made of one hydraulic cylinder attached to the WEC arm and connected to a four quadrant mode pump (located between the charge and overflow pipelines), which is used to control the movement of the cylinder during power extraction and reactive modes. This pump is attached to an electrical drive in order to convert the harvested energy into electrical one and to receive power from the same drive for reactive control. The torque of this drive is controlled in order to achieve a desirable speed which will push the pump displacement to its maximum displacement, and then, increasing its overall hydraulic efficiency. The control of this drive and its connection to the electrical grid is made with an inverter. However, this drive should be operated within some limits to avoid using too much electrical power to accelerate the generator. In this case, it was not allowed to work above 1000 rpm in motor mode and when the reference speed was determined in order to move the pump displacement to its maximum value (denominated speed strategy 4) [11]. This generator can also be controlled by (strategy 1) [11] fixing the speed according to each sea state, (strategy 2) [11] slowing varying the speed according to average peak and flow requirement and (strategy 3) [13] slowing working between strategies 2 and 4 (keeping trends from strategy 4 to improve efficiency). These last three strategies are less demanding than strategy 4, because the reference speed has a smoother variation, and so, with less abrupt accelerations of the electrical drive.

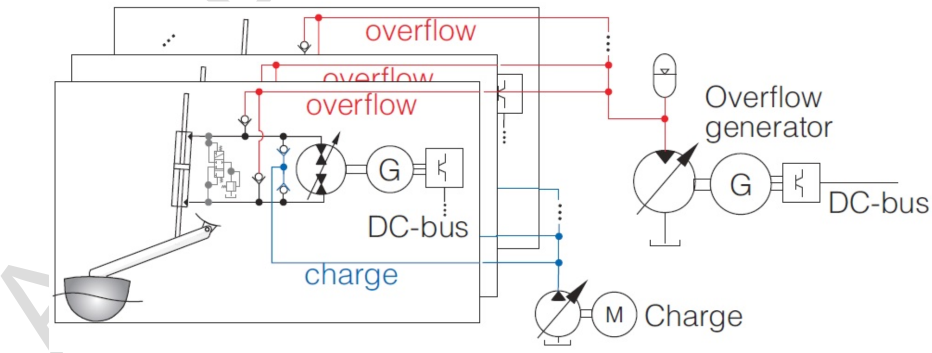

Figure 1. Power Take-Off [12].

A PTO concept based on two connected hydraulic pumps, instead of a pump and electrical drive, and known as the hydraulic transformer, has been presented by Gaspar et al. [13-16]. One of the objectives of this solution is to increase the maximum range of speed variations in order to move the first four quadrant mode pump to its full displacement, hence higher efficiency, and minimize the undermining effect on the efficiency of the second unit (the one that controls the transformer speed), known as back-to-back effect, e.g. the improvement of the efficiency of one pump decreases the efficiency of the other and vice-versa. Real time simulations were further carried out in a hardware-in-the-loop (HIL) test rig [13] with the objective of testing the four-speed control strategies and it was found that they require peak accelerations above 10000 rpm/s, which is above the ones supported by an AC and frequency controlled drive. So, the objective of this paper is to present a second study based on the same HIL approach in order to decrease the peak accelerations and power applied on an electrical drive connected to the four quadrant pump, and so, to determine if an AC frequency controlled motor could be used rather than an oil-hydraulic pump as the transformer second unit.

This paper is organized in five sections. In Section 2 the PTO concept and its main features are presented. The modeling of this PTO is presented in section 3 and the preliminary numerical simulations for three irregular sea states are presented in Section 4. These simulations were analyzed in order to set the requirements and set up the Tecnalia PTO test rig. The test results are then presented and discussed in Section 5 and summarized in the conclusion.

2. PTO Concept

The concept proposed by Gaspar et al. [13, 14], and presented in Figure 2, uses piloted-to-close valves (8 and 9) assembled in parallel with a hydraulic transformer (7 and 10) in order to bypass hydraulic power when the pressure on the high pressure side (unit 7) is above the one in the low pressure side (unit 10) and, on the other hand, to close the bypass gates during the reactive control operation and regardless of the differences between the two side pressures. So, during the wave power extraction phase only one part of the cylinder hydraulic power (1) goes to the transformer where it is converted into kinetic energy, which is later released and converted into hydraulic power by the same cylinder and to perform the WEC reactive control.

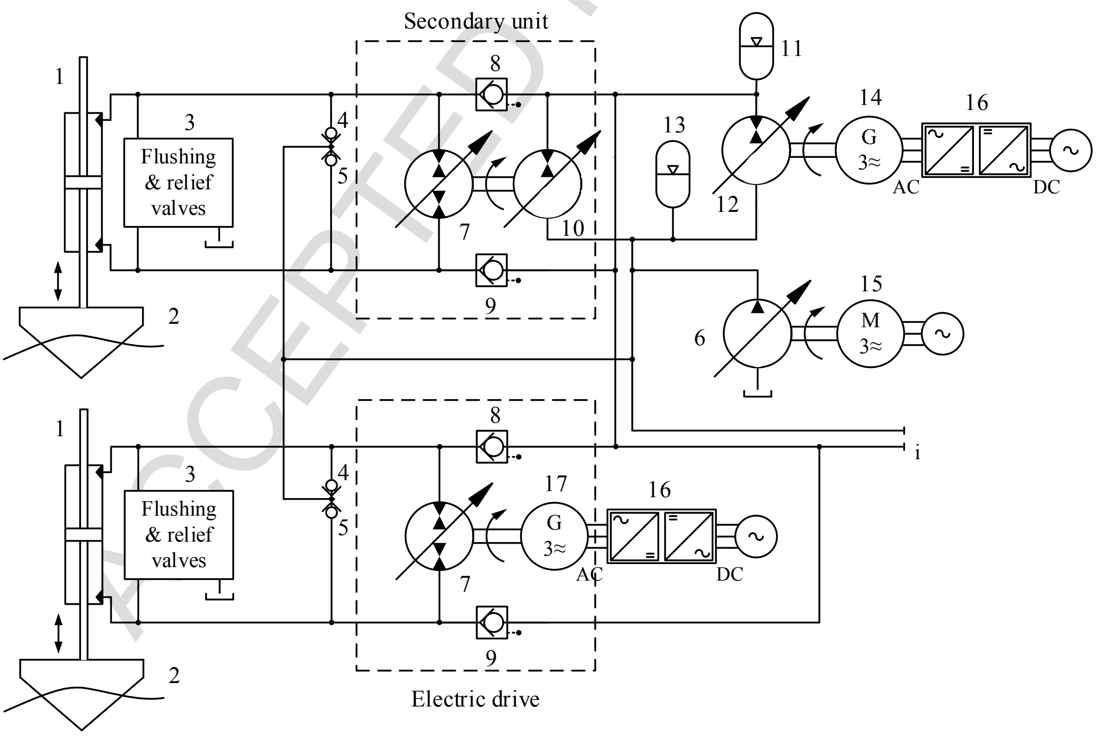

Figure 2. Hybrid version of a Power Take-Off concept for wave energy converters [13].

This bypass effect must be controlled in order to charge the transformer with enough kinetic energy for WEC reactive control (plus power losses) otherwise some of it will be transferred to the low pressure side via a second and inefficient hydraulic unit (10). This bypass fine tuning is carried out by controlling the average pressure difference between the two transformer sides, or in other words, the average differential pressure applied on the bypass valves. This can be carried out by controlling the low side pressure (pipeline *i*) with the pressure control pump (12). However, this solution adds an undesirable effect on the overall efficiency of this pump for reference pressures below 210 bar [13, 14]. Moreover, different reference pressures must be adjusted for different sea states, and this is not reasonable for the accumulators, which are designed for only one operating pressure. Then another solution is to set the same reference pressure of pipeline (*i*) for all sea states while changing the average pressure of the high pressure side by adjusting the reference pressure of the boost pump (6), or in other words, the pressure of the compensation flow entering in that circuit through compensation valves (4 and 5). This adjustment will move the average pressure applied on the bypass gate, in the high pressure side, down and up and according to the sea state. However, this also has a negative impact on all other pumps (10 and 12), because increasing boost pressure will also decrease the differential pressure applied on pumps 10 and 12, and so, decreasing their overall efficiencies. Then, a trade-off should be achieved by defining an upper limit on the boost pressure, from where the pump efficiencies can significantly drop.

3. WEC modelling

The design of a reliable drive control strategy is only achievable by taking into consideration the system losses and constraints [17-18]. This is even more important when active control is implemented in order to extract more power from the waves [19]. As a consequence, this involves the increment of the model fidelity but also a significant increase on its complexity, which might undermine the design process. So, a balanced approach to these two design requirements was sought during the modelling phase. However, full fidelity was achieved in the drive part, by including it, and associated control and back-to-back converter equipment, as embedded components in a HIL test rig [13]. This assured that at least the main object of this study was analyzed with the complexity that a numerical model hardly achieves and without undermining the design process.

So, the wave, WEC floater hydrodynamics and PTO models were simulated in the test rig [13, 20-22], with the objective of analyzing the impact of the speed control strategies and pump boost pressure on the speed and acceleration of the PTO electrical drive (components 16 and 17 in Figure 2). These models were adapted from [13] and for the same sea state conditions. However, a hydraulic cylinder with a saturation force of 500 kN was used instead of the original one (420 kN) in order to evaluate if the variation on the boost pressure works well for a higher extracted wave power.

3.1. Hardware-In-the-Loop model simulation

The experimental tests were made on the Tecnalia electrical PTO test rig [22], as presented in Figures 3 and 4.

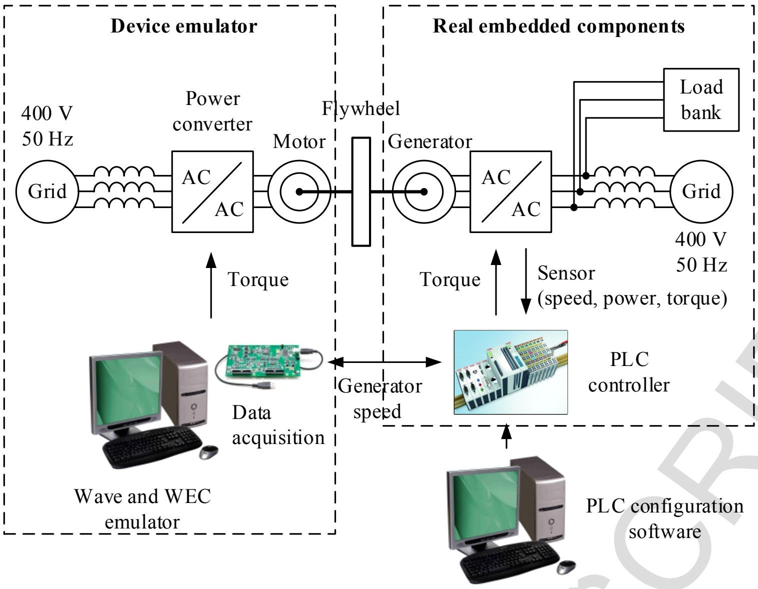

Figure 3. Tecnalia Electrical PTO lab test rig (adapted from [13, 20-22]).

The Wave2Wire (W2W) numerical model was developed on a Host computer in the Matlab/Simulink environment (Figure 3, Wave and WEC emulator). It was then compiled into a real time application and downloaded to the Target PC. This computer was equipped by a real time processing board, in charge of the data acquisition, and connected to an I/O terminal board. It was operated by a real time operating system which executed the W2W code.

The HIL was setup so that two analogue outputs and one analog input connected the Target PC and the test rig. As for the outputs, one was the motor torque reference signal sent to the power converter (Figure 3, left side); and the other the reference speed signal to the PLC. The PLC then controls this reference by a PI-controller by adjusting the generator resistive torque. This reference torque is then sent to the second power converter (Figure 3, right side) where it is equivalent current value is controlled by another PI-controller. The two signals represent, as regards to the oil-hydraulic equivalent circuit (Figure 2), the torque applied by the first transformer unit (component 7) on the secondary one (component 17), and the speed reference given to the controller of the secondary unit (component 16), respectively. On the other hand, the analog input signal was the feedback test rig rotational speed, which was sent back to the W2W model, and so, affecting its response.

The test rig motor and generator were mechanically connected with a shaft while a 1 kgm2 flywheel was attached to increase the system inertia. The flywheel smooths the reciprocating motion of the pump internal pistons and stores rotational energy.

The test rig motor was a Leroy-Somer, 2 pair poles, squirrel cage and induction motor of a nominal power of 15 kW and nominal and maximum speeds of 1460 rpm (50 Hz) and 1800 rpm, respectively. It was controlled by a frequency controller of the same manufacturer. The ABB generator was also a squirrel cage induction generator but with a nominal power of 11 kW, nominal speed of 768 rpm (50 Hz) and maximum speed of 1000 rpm. This generator was connected to the grid by an ABB back-to-back bidirectional (frequency) converter. The gearbox (component 2 in Figure 4) was removed from the test rig.

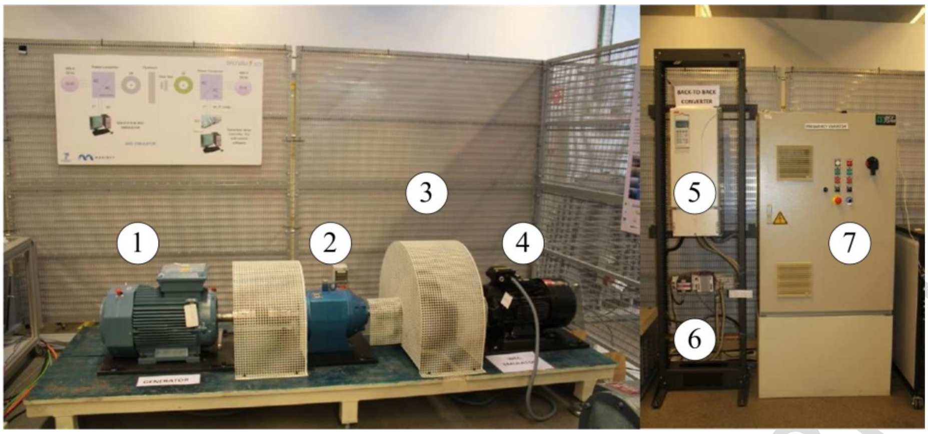

Figure 4. PTO test rig. Legend: (1) Motor, (2) gearbox, (3) flywheel, (4) generator, (5) generator power converter, (6) PLC and (7) motor power converter.

3.2. PTO control strategies

This research study made use of the same drive speed control strategies tested by Gaspar et al. [13], two from the state-of-the-art (St2 and St4) [11] and one (St3) presented by the same author [13]. The St2 strategy calculates a reference speed that slowly works between its peak and average values while St4 calculates highly variable speed reference values. Strategy St3 slowly works between the previous two strategies. The speed calculation algorithm of these strategies is presented in [13].

The differences between these speed control strategies are illustrated in Figure 5. The St1 strategy is the most basic one and is included here for comparative analysis. As revealed in the same figure, the variation in speed increases from St1 to St4, meaning that for the same pump power (component 7 in Figure 2) its displacement gets closer to 100 %, and so, to maximum pump efficiency. The influence on the secondary unit, in this case, an electric drive, is not directly affected if the applied torque is above half of the maximum load supported by the drive. However, and in particular in St4, the lifetime of the pump and electrical drive components may be reduced. Moreover, according to [11], an electrical drive working at St4 will require substantial electrical power, when working as a motor, in order to accelerate the generator inertia and achieve the reference speeds. So, Hansen et al. [11] set a speed limit of 1000 rpm for the motor mode.

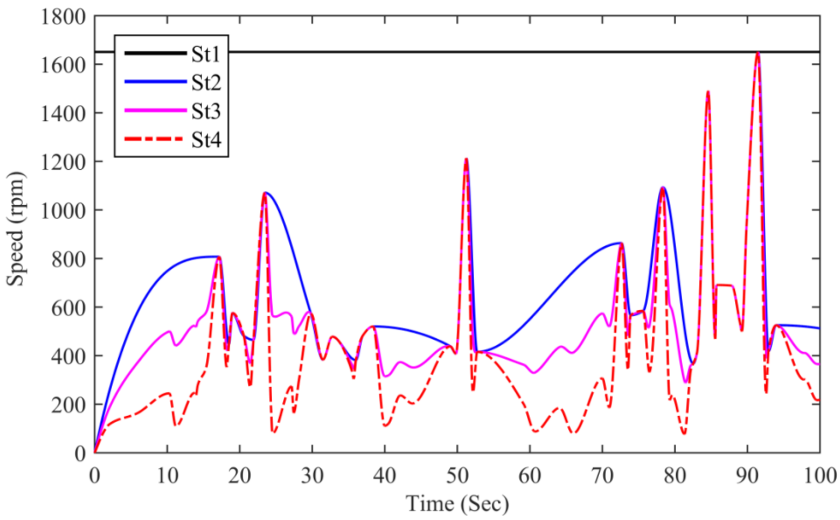

Figure 5. Speed control strategies [13].

In the present case study, the flywheel inertia is used to store enough kinetic energy for reactive control of the WEC. This brings an additional benefit for the secondary electrical drive, which is to avoid working as a motor and consuming too much electrical power from the grid. On the other hand, these high speed fluctuations can be too much for the test rig electrical motor, which might be impossible to achieve because of the required accelerations.

The speed control strategy St4 was also implemented in the second electrical generator presented in Figure 2 (component 14), because the power fluctuations are smoother at this part of the hydraulic circuit due to the use of oil-hydraulic accumulators (represented by an equivalent accumulator, 11 in Figure 2). However the control of the pump (component 12 in Figure 2) attached to this drive was carried with a different approach based on fuzzy logic control, as presented in Figure 6.

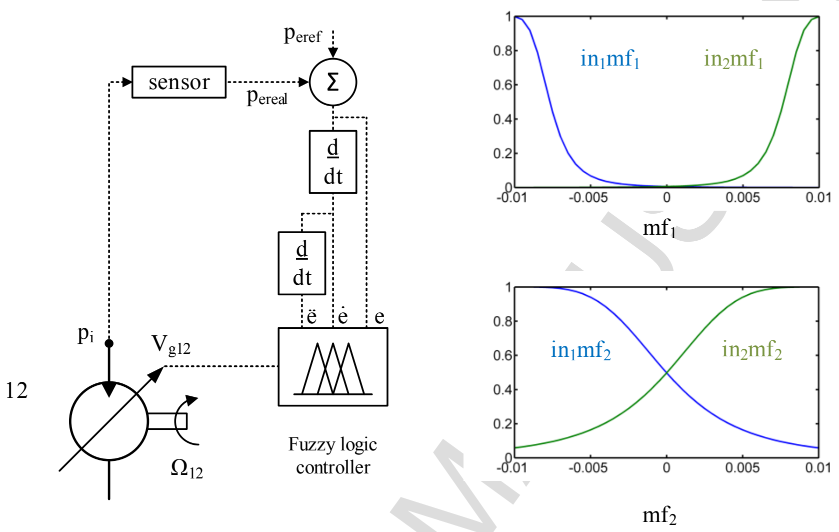

Figure 6. Fuzzy logic based pressure control system. Membership functions: mf_1 for error (e), mf_2 for $\dot{e}$ and mf_3 (profile is the same as mf_2) for $\ddot{e}$ [13].

The reference pressure p_{eref} was set to 210 bar and compared with the real pressure p_{real} given then an resulting error (e), which was then processed ($\dot{e}$ and $\ddot{e}$) with two differentiators. Then these three signals were sent to the Fuzzy logic controller where eight if-then rules were employed. One of these rules was, for example: If (e is in_1mf_1) and ($\dot{e}$ is in_3mf_1), then (Δ is out_1mf_1). For a more detailed explanation of the basic laws behind the rules of this fuzzy logic controller see [13]. The selected reference pressure (210 bar) is the one that guarantees the best overall efficiency of the hydraulic pumps (efficiency decreases significantly below this pressure level [14]) and an economical installation, since higher levels of pressure increase the quantity of used steel (e.g. piping and accumulator wall thickness).

3.3. Oil-hydraulic system

The following formulation, regarding Figure 2, was developed [13] in order to calculate the two real time signals, which were sent to the test rig, the generator reference speed (component 4 in Figure 4) and the motor torque (component 1 in Figure 4). The reference speed is determined with:

$$\Omega_{17} = \Omega_{10} = \frac{6E5P_7}{V_{g7max}\Delta_{p7}} \qquad (1)$$

where $\Omega_{17}$is the rotational speed of the generator, and V_{g7max} [cm^3/rot] and Δp_7 [bar] are the pump maximum displacement and applied differential pressure, respectively. Moreover, the pump hydraulic power P_7 [kW] is given with:

$$P_7 = (P_1 - P_8\eta_8) \quad (2)$$

$$P_1 = F_1\dot{x}_c\eta_1(d, d_r, \Delta_{p1}, c_p) \quad (3)$$

$$P_8 = \Delta p_8 Q_8/(600\eta_8(\Delta p_8, Q_8)) \quad (4)$$

where P_1 [kW] is the cylinder hydraulic power, F_1 is the force applied on the cylinder rod, $\dot{x}_c$ is the cylinder speed and η_1 is the cylinder mechanical efficiency determined according to piston diameter (d), piston diameter ratio (d_r) (ratio between the piston and rod diameter), applied differential pressure (Δp_1) and the performed function (c_p) (e.g. pushing or pulling). The cylinder volumetric efficiency was considered as 100%. On the other hand, P_8 (or P_9) is the hydraulic power directly bypassed into the pipeline (i) via the pilot-to-close non-return valve 8 (or 9), $\Delta p_8 = F_1/A_1 + p_6 - p_{11}$ [bar] is the valve applied differential pressure, A_1 is the piston area, p_6 is the boost pressure and p_{11} is the oil pressure inside the accumulator (no losses in the pipeline were considered). The valve efficiency, η_8, and hydraulic flow, Q_8 [L/min], are determined with:

$$\eta_8 = (\Delta p_8 - \Delta p_{8ploss})/\Delta p_8 \quad (5)$$

$$\Delta p_{8loss} = 2 \cdot 10^{-6}Q_8^3 + 2 \cdot 10^{-4}Q_8^2 + 65 \cdot 10^{-4}Q_8 + 0.48 \quad (6)$$

$$Q_8 = C_d A_8\sqrt{\frac{2}{\rho_f}}\Delta p_8^{1/2} \quad (7)$$

where Δp_{8ploss} is the valve pressure loss, C_d is the valve discharging coefficient, A_8 is the valve orifice area and ρ_f is the oil density.

The second real time signal, the motor torque, is determined with:

$$T_{17} = T_{10} = \frac{V_{g10}\Delta_{p10}}{20\pi} \quad (8)$$

where T_{17} is the generator torque, and V_{g10} and Δp_{10} are the pump maximum displacement and applied differential pressure, respectively. The pump displacement is determined with:

$$V_{g10} = \frac{6E5P_{10}}{\Omega_{10}\Delta_{p10}} \quad (9)$$

where the power in the secondary pump (10) is given with:

$$P_{10} = \frac{1}{\Delta t}\int_{t_1}^{t_2} P_7(t)\eta_7(\Delta p_7, \Omega_7, V_{g7})dt \quad (10)$$

where $\Delta t = t_2 - t_1$ is the simulation time, η_7 is the overall efficiency of the four quadrant mode pump, which was determined as a function of the unit differential pressure (Δp_7), speed (Ω_7) and displacement (V_{g7}). On the other hand, the pump applied pressure Δp_{10} is determined with [13, 23, 24]:

$$\Delta p_{10} = p_{11} - p_6 \quad (11)$$

$$\dot{p}_{11} = \left[Q_{11} + (T_w - T)V_{g11}(T\tau_c)^{-1}\left(1 + \frac{R}{c_v}\right)^{-1}\right] \Big/ \left[\frac{V_{g11}}{p_a}\left(1 + \frac{R}{c_v}\right)^{-1} + \frac{n_{11}V_{0g11} - V_{g11} + V_{ext}}{\beta_{eff}}\right] \quad (12)$$

and

$$\tau_c = m_g L\sigma_g F^{-1.760}T^{*2.528}\left[\rho_g^2 g L^3(T - T_w)\right]^{-0.344}/(1.6151A_w) \quad (13)$$

where $\dot{p}_{11}$ is the rate of change of accumulator pressure p_{11}, T_w and T are the accumulator wall and gas temperatures, respectively, V_{g11} and V_{0g11} are the accumulator initial gas and size volumes, respectively, R is the ideal nitrogen constant, c_v is the nitrogen specific heat at constant volume, n_{11} is the quantity of accumulators and β_{eff} is the fluid bulk modulus in the pipeline. Moreover τ_c is the accumulator thermal time constant, m_g is the nitrogen mass, L is the cylinder length in contact with the gas, A_w is the cylinder internal area exposed to the gas, ρ_g is the gas density, g is the gravity acceleration, T^* is the ratio of wall (T_w) to gas temperature (T), σ_g is a function of gas properties and F is a function of the accumulator geometric properties according to [24]. The boost pressure, p_6 was considered as constant with a reference value of 10 bar, the minimum pressure in these type of pumps [25]. On the other hand, the accumulator hydraulic flow, Q_{11}, is determined with:

$$Q_{11} = N_{PTO}(Q_{8-9} + Q_{10} + Q_{12}) \quad (14)$$

$$Q_{10} = 600P_{10}\eta_{10}(\Delta p_{10},\Omega_{10},V_{g10})/\Delta p_{10} \quad (15)$$

$$Q_{12} = \Omega_{12}V_{g12} \quad (16)$$

where N_{PTO} is the number of PTOs, Q_{10} and Q_{12} are the hydraulic flows of pumps 10 and 12, respectively, and Ω_{12} and Vg_{12} are the speed and displacement of pump 12, respectively. On the other hand, the reference speed of pump 12 is determined with the objective of operating at its maximum overall efficiency, as follows:

$$\Omega_{12} = 6E5\overline{P}_i/(V_{g12max}\overline{p}_{12}) \quad (17)$$

$$\overline{P}_i = \frac{N_{PTO}}{\Delta t}\int_{t_1}^{t_2} P_i(t)dt \quad (18)$$

$$P_i = P_8 + P_9 + P_{10} \quad (19)$$

$$\overline{p}_{12} = \frac{1}{\Delta t}\int_{t_1}^{t_2} p_{12}(t)dt \quad (20)$$

where V_{g12max} is the maximum pump displacement, P_i and $\overline{P_i}$ are the pipeline instantaneous and averaged hydraulic powers, respectively, and p_{12} and $\overline{p_{12}}$ are the pump instantaneous and averaged pressures.

The determination of the cylinder and pump efficiencies are made with the same models developed in [13], which are based on the Adaptive Neuro Fuzzy Inference System (ANFIS) [26, 27]. The performance of these models was acceptable. The cylinder efficiency model had a Root-mean-square deviation (RMSE) of 0.0068 and R-squared (R^2) of 0.88 while the pump efficiency model had an RMSE of 0.6463 and R^2 of 0.9980. The RMSE value was reasonably low as compared with the work presented in [28], and the R^2 indicator was used to evaluate the models forecasting performances. On the other hand, the non-return valve and generator efficiency models were created with polynomial approximations ($R^2 = 0.99$) of the original curves and data given by manufacturers [29, 30] in the same way as presented in [13].

3.4. Point floater WEC hydrodynamics and wave model

The cylinder hydraulic power, P_1 (see Equation 3), is determined by the force applied to the cylinder rod (F_1) and its stroke speed ($\dot{x}_c$). The cylinder force is calculated with [6] (see Figure 7):

$$F_1 = M_{PTO}(t)/l_1 \quad (21)$$

$$l_1 = \frac{l_2 l_3 \sin(\theta - \alpha_0)}{(x_c + l_4)} \qquad (22)$$

$$x_c = -l_4 + \sqrt{-2 l_2 l_3 \cos(\theta - \alpha_0) + l_2^2 + l_3^2} \qquad (23)$$

where $M_{PTO}(t)$ is the moment applied on the WEC arm by the hydraulic cylinder rod, l_1 to l_4 are the distances between the WEC joints as presented in Figure 5, α_0 is the initial arm angle, and x_c is the cylinder stroke. θ is the angle of the float arm, where the $\theta = 0$ corresponds to the float position at rest.

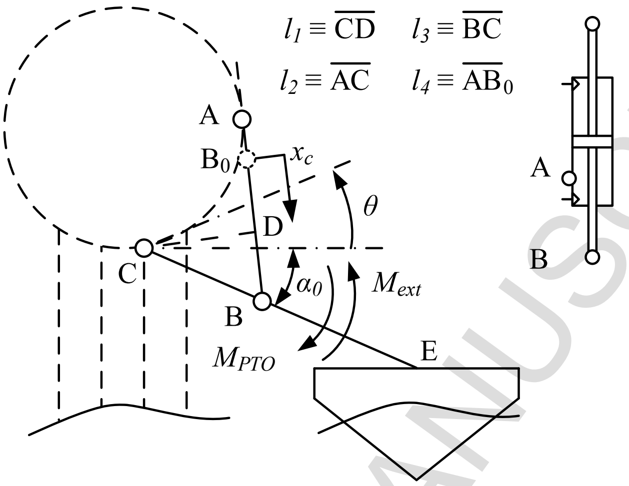

Figure 7. Cone-cylinder floater WEC (adapted from [6, 13]).

The applied $M_{PTO}(t)$ is determined according to a control scheme [13] which takes as the reference value:

$$M_{PTO,ref}(t) = k_{PTO}\theta(t) + b_{PTO}\dot{\theta}(t) \qquad (24)$$

and the system to control (see Appendix A):

$$(J + J^{\infty})\ddot{\theta}(t) + \int_0^t k(t-\tau)\dot{\theta}(t) + k_{res}\theta(t) = \int_{-\infty}^{\infty} h_{e\eta}(t-\tau)\eta_w(\tau)d\tau \qquad (32)$$

where k_{PTO} is the spring constant, b_{PTO} is the damping coefficient, J is the moment of inertia of the float and arm, J^{∞} is the added mass at infinite frequencies, $k(t)$ is a time dependent retarded function, τ is the time delay, k_{res} is the hydrostatic stiffness coefficient and $h_{e\eta}$ $(t - \tau)$ is the impulse response function of the excitation moment, determined with Boundary Element Method (BEM) software package WAMIT [31]. On the other hand, the undisturbed wave elevation time-series at the float center, $\eta_w(\tau)$, were determined for three sea states with specific wave heights (H_s) and peak wave periods (T_p) of - SS1 (H_s = 1m, T_p = 4.62s), SS2 (H_s = 1.75m, T_p = 5.57s) and SS3 (H_s = 2.50m, T_p = 6.44s), as in [6], with:

$$\eta_w(t) = \sum_{i=1}^{n} \sqrt{2 S_{\xi_A}(f_i)\Delta f}\,\sin(2\pi f_i t + \varphi_{rand,i}) \qquad (33)$$

which was developed by superimposing the i individual wave components:

$$\eta_{w,i}(t) = \sqrt{2 S_{\xi_A}(f_i)\Delta f}\,\sin(2\pi f_i t) \qquad (34)$$

extracted with the parameterized JONSWAP wave amplitude spectrum [32]:

$$S_{\zeta_A}(f) = \alpha_s H_s^2 f_p^4 f^{-5} \gamma^{\beta_s} \exp\left(\frac{-5}{4} \left(\frac{f_p}{f} \right)^4 \right) \quad (35)$$

where:

$$\alpha_s = \frac{0.0624}{0.230 + 0.0336\gamma - \left(\frac{0.185}{1.9 + \gamma} \right)} \quad (36)$$

$$\beta_s = \exp\left(-\frac{(f - f_p)^2}{2\sigma^2 f_p^2} \right) \quad (37)$$

$$\sigma = \begin{matrix} 0.07 & \text{for} & f < f_p \\ 0.09 & \text{for} & f \geq f_p \end{matrix} \quad (38)$$

where γ is the peak enhancement factor ($\gamma = 3.3$), f_p is the peak frequency, σ is the value of the spectral width and $\varphi_{rand,i}$ is a random phase for each component.

The wave spectra and correspondent wave elevation time-series for all sea state conditions are presented in Figures 8 and 9, respectively.

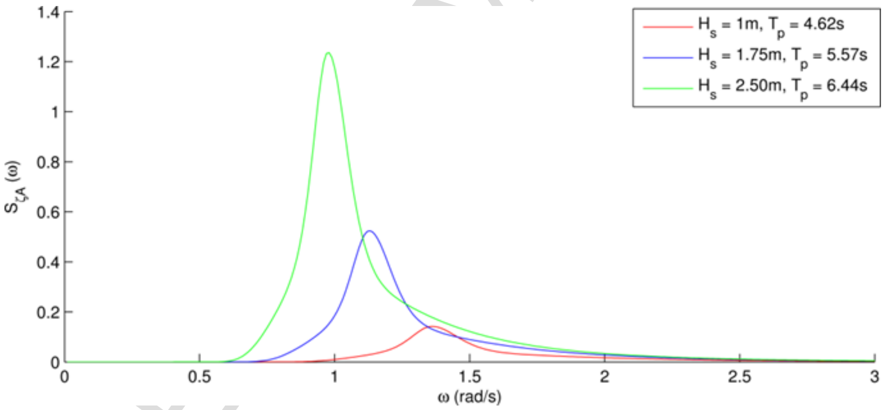

Figure 8. Wave spectra for different sea states [13].

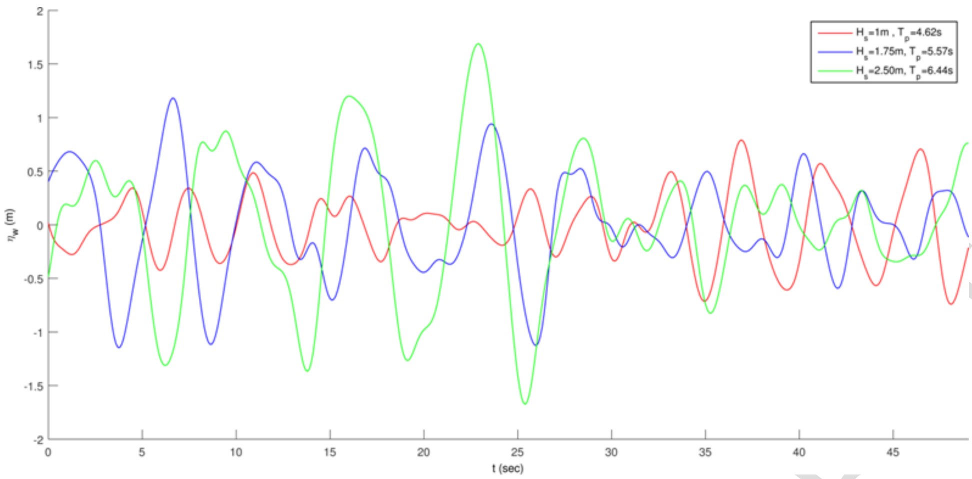

Figure 9. Wave elevation time-series for three different sea states [13].

4. Experiment calibration and setup

The full PTO numerical model (at prototype scale) was simulated in first place, to determine the power requirements of the electrical generator (component 17 in Figure 2) in order to integrate it with the test rig (at model scale). The integration was made by scaling down the torque and speed references, determined with the numerical simulation, and sending them to the motor and generator controllers. On the other hand, the real torque and speed signals, measured at the test rig, were scaled up and sent to the same numerical simulation. The generator nominal power requirements are presented in Table 1, for the two scenarios, when the boost reference is not changed (Type I) and changed (Type II) according to each sea state. In the first case (Type I) the boost pressure is 38 bar and the cylinder pressure is 350 bar, which is the maximum admissible pressure of a mill type hydraulic cylinder [33] with 200 mm and 140 mm of cylinder piston and rod diameters, respectively.

In the second scenario (Type II), the boost pressure increases for less energetic sea states, 10 bar (SS3), 35 bar (SS2) and 50 bar (SS1), in order to compensate the loss in the cylinder average pressure. Moreover, the maximum pressure is now 480 bar, which is far above the admissible ones of standard mill cylinders. This maximum pressure is achieved with a reduction in the cylinder annular area, and so, with a smaller piston diameter of 180 mm and regulating the relief valves (component 3 in Figure 2) to open at 480 bar. So, this cylinder should be designed to support this level of pressure, despite using standard piston and rod diameters (the rod diameter is not changed in order to support 500 kN of maximum force). With this second solution (Type II), the average power at the electrical drive is much lower than in the first situation (Type I), which indicates a more efficient use of the kinetic energy for WEC reactive control. This solution is also more efficient for a hydraulic transformer (components 7 and 10 in Figure 2), because the impact of the unit (10) inefficiency on the overall efficiency is minimized, i.e. fewer power losses than in Type I scenario.

Table 1. Generator power requirements at the prototype scale.

Scenario	SS	Power [kW] [1)]		Pressure [Bar]		Cylinder [mm]	
		Average	Std.	Max.	Boost	Piston	Rod
I	1	0.79	0.06	350	38	200	140
	2	4.10	0.23	350	38	200	140
	3	10.4	0.47	350	38	200	140
II	1	0.15	0.02	480	50	180	140
	2	1.50	0.02	480	35	180	140
	3	2.72	0.23	480	10	180	140

[1)] Power calculated for a time-series length of 30 minutes (1800s)

The maximum average simulated power at the prototype scale, according to Table 1, was 10.87 kW (10.4 + 0.47 kW) (Type I, SS3), which is not far from the nominal power of a commercial electrical generator of 11 kW (same nominal power of the test rig generator). This corresponds to a scale length of [13, 20, 34, 35]:

$$\varepsilon = (P_{17,m,nom}/P_{17,p,nom})^{2/7} = (11/10.87)^{2/7} = 1.0034 \qquad (39)$$

where $P_{17,m,nom}$ and $P_{17,m,nom}$ are the nominal generator power at the model and prototype scales, respectively. So, the generator model and prototype were considered as the same ($\varepsilon = 1$), however, the maximum admissible torque and speeds of the test rig generator were inferior to the ones at the model level. Then corrections have to be made with (see Appendix B):

$$\Omega_{17} = r\Omega_{17,m} = r\Omega_{17,p}\varepsilon^{-1/2} = (\Omega_{17,nom}/\Omega_{17,m,nom})\Omega_{17,p}\varepsilon^{-1/2} \qquad (40)$$

where $\mathbf{\Omega}_{17}$ is the test rig generator speed, r (768/3000) is the speed correction factor, $\mathbf{\Omega}_{17,m}$ is the generator speed at the model level, $\mathbf{\Omega}_{17,p}$ is the generator speed at the prototype scale, $\mathbf{\Omega}_{17,nom}$ is the nominal speed of the test rig generator and $\mathbf{\Omega}_{17,m,nom}$ is the nominal speed of the generator at model scale. On the other hand, the reference torque sent to the electrical motor (component 7 in Figure 2) is adjusted with (see Appendix B):

$$T_M = r\varepsilon^{-1}\frac{I}{I_{7,p}}T_{7,p} \qquad (56)$$

where T_M and $T_{7,p}$ are the motor reference torques at the test rig and prototype levels, respectively, and I and $I_{7,p}$ are the motor inertias in test rig and prototype levels, respectively. The prototype inertia ($I_{7,p}$) was adjusted for each sea state test conditions and speed control strategy.

The same controller proportional (P = - 0.6) and integrative (I = - 0.3) gains, as in [13], were used in this experiment and the cone-cylinder floater (Figure 1) had an apex angle of 90º and a diameter of 5 meters extended by a cylindrical part of 0.5 meters, which gave a total equilibrium draft of 3 meters [36]. The PTO model parameters are presented in Appendix C.

5. Results

The test results were obtained from a statistical analysis made on data collected during a 10 minutes simulation time, because at the end of this period the generator operation was already stable. Some exceptions are presented in Table 2, in speed strategies St2 (SS3) and St4 (SS1 and SS2). These three tests were carried out approximately between 2 to 4 minutes, because it was not possible to set drive inertia in order to operate the generator at the minimum possible rotation speed, which in these three cases was 105 RPM. The objective of all these tests was to set the device in order to follow the reference speed to its minimum without causing the test rig shutdown and covering, as possible, the maximum variation in the reference speed. This was successfully made for all other strategies and sea state conditions without using an auxiliary cooling system, which could remove the generator heat at lower rotation speeds. So, this means that better results could be achieved with a ventilation system and setting a limit on the minimum generator reference speed. Table 2 also reveals that higher speed errors can be found on the same three identified tests (169, 135 and 96 rpm).

Table 2. Generator speeds - Type I simulation.

Control strategy	SS	Real speed [rpm][a)]				Error [rpm] [b)]		
		Min.	Max.	Range	Average	Average	Std. Dev.	Max.
Slowly working between speed peaks and average values (St2)	1	551	1996	1445	898	45	69	458
	2	520	1785	1266	926	45	108	808
	3	105	1277	1172	926	**169**	146	727
Slowly working between strategies 2 and 4 (St3)	1	309	1340	1031	672	**123**	196	1127
	2	656	2977	2320	1227	77	92	1023
	3	367	1781	1414	766	50	62	1000
Working with highly variable speed reference values (St4)	1	105	1277	1172	645	**135**	139	1362
	2	105	2699	2594	660	**96**	127	1362
	3	1895	2824	930	1344	73	185	1835

[a)] These results were collected for a 10 minutes time simulation with exception of St2-SS3 (1.77’), St4-SS1 (1.55’) and St4-SS2 (3.53’).
[b)] Difference between the generator reference and real speeds (highest differences are bold highlighted).

According to Table 2 it is not possible to use the 250 cm^3 hydraulic motor in St3 (SS2) and St4 (SS3) to drive the generator, because the maximum speeds are above the ones of the motor, which is 2700 rpm at full displacement. Moreover, the range of speed variations is also very demanding, practically above 1000 rpm in all cases, and can achieve 2320 (St3-SS2) and 2594 (St4-SS2) rpm in extreme cases.

The results of the Type II simulation tests are presented in Table 3. In contrast to the previous Type I simulation, the tests were successfully carried out for a time length of 10 minutes. Moreover, it was possible to operate the generator for lower speeds between 31 to 113 rpm at the most extreme sea state conditions (St4) and without shutting down the test rig. The maximum generator speeds were also below the permissible limit of 2700 rpm, with a slight increase in St2-SS2 (2707 rpm), which guarantees the correct operation of the 250 cm^3 hydraulic motor. The range of speed variation is also high but not so demanding, because the averaged speed error (in overall) is lower than in Type I simulations (Table 2).

Table 3. Generator speeds – Type II simulation.

Control strategy	SS	Speed [rpm][a)]				Error [rpm]		
		Min.	Max.	Range	Average	Aver.	Std.	Max.
Slowly working between speed peaks and average values (St2)	1	539	1758	1219	762	31	35	327
	2	926	2707	1781	1254	39	73	1273
	3	328	1656	1328	668	42	100	908
Slowly working between strategies 2 and 4 (St3)	1	180	1758	1578	656	42	42	712
	2	535	2316	1781	1031	92	177	1742
	3	285	1805	1520	570	50	73	719
Working with highly variable speed reference values (St4)	1	113	1527	1414	496	85	77	473
	2	31	2344	2313	770	54	123	888
	3	82	2590	2508	695	135	192	1469

[a)] These results were collected for a total time simulation of 10 minutes.

The results presented in Table 3 point to, in overall, an increment on the generator speed range from strategies St2 to St4, and so, pushing the hydraulic motor to full displacement and higher operation efficiencies. However, a 3000 rpm, 2 pole, generator must be used in order to run at the maximum simulated speeds (2707 rpm in Type II simulation).

A second analysis was made on the same speed data in order to analyze the generator peak accelerations and dynamic response. The results are presented in Table 4 for Type I and II simulations as well as the reference and real speed signals.

Table 4. Maximum generator acceleration - Type I and II simulations.

Control strategy	Sea state	Peak acceleration [1x10^4 rpm/s]		Acc. above 1x10^4 rpm/s [%]	
		I [ref. | real]	II [ref. | real]	I [ref. | real]	II [ref. | real]
Slowly working between speed peaks and average values (Strategy St2)	1	3.29 | 1.89	4.49 | 1.05	0.00 | 0.09	0.00 | 0.00
	2	6.27 | 1.11	9.39 | 1.19	0.02 | 0.00	0.00 | 0.00
	3	1.62 | 2.53	6.05 | 1.39	0.00 | 0.12	0.01 | 0.01
Slowly working between strategies 2 and 4 (St3)	1	4.60 | 1.73	5.27 | 2.06	0.01 | 0.09	0.04 | 0.01
	2	11.2 | 2.93	9.63 | 1.41	0.02 | 0.12	0.03 | 0.05
	3	7.82 | 1.74	3.85 | 1.49	0.03 | 0.01	0.01 | 0.01
Working with highly variable speed reference values (Strategy St4)	1	8.38 | 1.45	3.99 | 1.30	0.00 | 0.12	0.01 | 0.02
	2	6.75 | 2.24	2.56 | 2.63	0.01 | 0.21	0.05 | 0.02
	3	12.9 | 2.12	4.25 | 1.92	0.15 | 0.07	0.01 | 0.09

According to Table 4 the real peak accelerations are below the reference ones, except St2-SS3-I and St4-SS2-II, showing then the generator limitations to follow the speed reference signals. Moreover, these peak accelerations are above 1x10^4 rpm/s, which is by itself the maximum acceleration achievable by an AC frequency controlled motor. However, the peak accelerations above this limit are rare as presented on the right side of Table 4, in the percentage of the total computed accelerations. In particular the proportion of Type II real peak accelerations are lower than the ones of Type I simulations.

The drive flywheel inertia $I_{7,p}$ (Equation 56) was adjusted, in the numerical part of the simulation, in each test in order to maximize the generator response to the variations on the speed reference signal. Some of the results achieved with these adjusted inertias are presented in Figure 10 for Type II simulations and for a period of time between the 7th (420 s) and 9th (540 s) simulation minutes. The inertia adjustments are presented in Table 5.

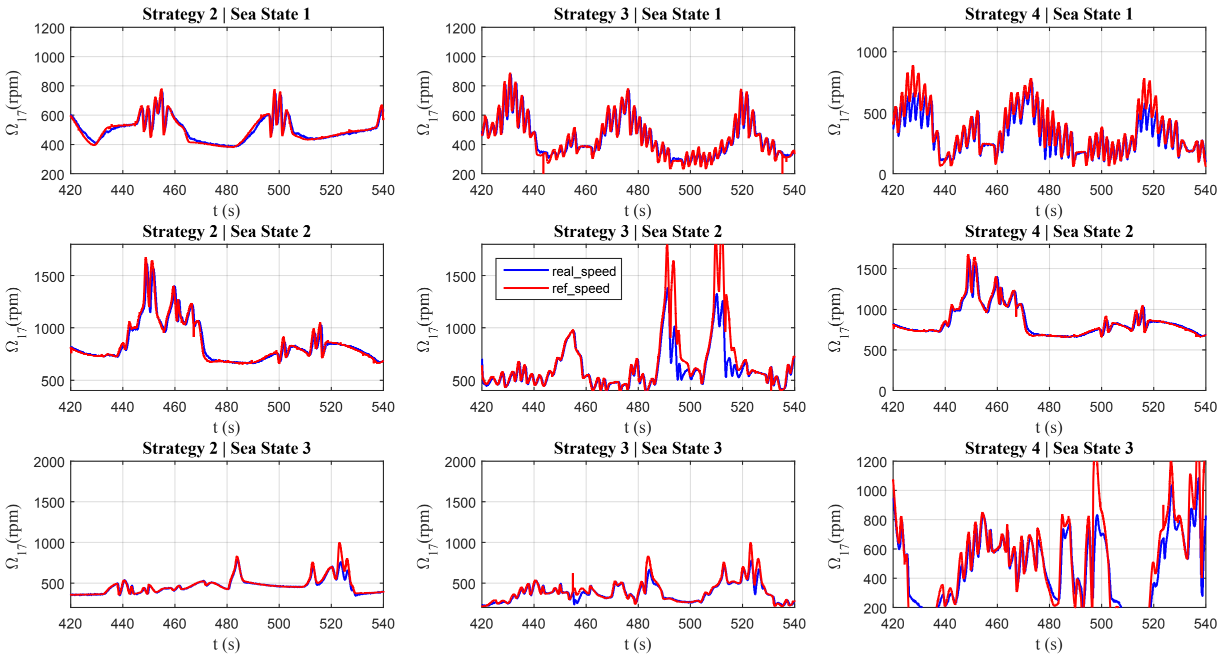

Figure 10. Reference and real electrical drive for different control strategies and sea states.

As revealed in Figure 10, the generator dynamic response is problematic in strategy 3, SS2 (middle of the figure), in two reference speed peaks located between 480 and 520 rpm and in strategy 4, SS3 (bottom right figure) in a speed peak located at 500 s. However, the generator response is acceptable for less extreme amplitude speed peaks, which occur most of the time in all the presented strategies and sea states.

Table 5. Speed control strategy adjusted drive inertias - Type II simulations.

Control strategy	SS	Inertia [Kgm^2]	Flywheel [Kg]
Slowly working between speed peaks and average values (St2)	1	2.2	53
	2	2.2	53
	3	6.0	127
Slowly working between strategies 2 and 4 (St3)	1	2.2	53
	2	6.0	127
	3	6.0	127
Working with highly variable speed reference values (St4)	1	4.4	106
	2	6.0	127
	3	4.4	106

As presented in Table 5, the drive inertia must be added or subtracted according to the sea state conditions. This can be made with two flywheels in each speed control strategy, as presented in Figure 11. For example, if the final design decision is to select a PTO controlled with strategy St3, then one flywheel of 2.2 kgm^2 (component 3 in Figure 7) must be fixed at the middle of the shaft, where the hydraulic motor and generator are attached, while the second one of 3.8 kgm^2 (14) is attached to the hydraulic motor through drive (12) with a clutch (11) in order to provide the 6 kgm^2 for SS2 and SS3. However, this requires heavy flywheels as shown in Table 5.

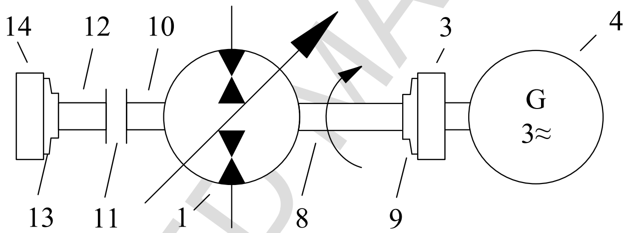

Figure 11. PTO electrical drive. Legend: (1) Hydraulic motor, (3) flywheel for SS1, (4) generator, (8, 10 and 12) drive shaft, (9 and 13) flywheel coupling, (11) clutch, (14) flywheel for SS2 and SS3.

The flywheel inertias were adjusted in order to take into consideration the components presented in Figure 7. This adjustment was carried out with the support of manufacturer technical sheets [25, 29, 37, 38] and the formulation presented in [13]. The adjusted inertias were approximately 1.94 and 3.73 kgm^2 for the first and second flywheels, which corresponds to 54 cm and 64 cm of flywheel diameter, respectively.

6. Conclusion

The numerical simulations have shown that adjusting the PTO boost pressure according to each sea state condition contributes to the increment of the hydraulic flow through the bypass valves, and so, leads to the reduction of the power delivered to the motor-generator drive. Then the boost pressure reference was fine-tuned in order to charge the motor-generator drive with enough kinetic energy for reactive power and to overcome the drive power losses. As a result of this approach and in contrast to the one where the boost pressure is constant, all control strategies could be implemented in the test rig during the simulation time length and the generator could operate at lower speeds between 31 to 113 rpm at the most extreme sea state conditions. Moreover, the maximum generator speed was always below the admissible limit of 2700 rpm and the speed range variations were higher, hence pushing the hydraulic motor to work near full displacement and with higher efficiencies.

This research work also revealed the generator limitations to accelerate to reference levels well above 1x10^4 rpm/s, which is easily achievable with a hydraulic pump when used instead of an electrical generator. However, peaks above 1x10^4 rpm/s are so rare that the employ of a generator does not undermine the efficiency of the hydraulic motor. On the other hand it is much cheaper than a hydraulic pump, which is designed for higher power levels.

So, the most economical solution is to use a hydraulic motor – electric generator drive, however, it brings with it additional difficulties, which are the customization of a hydraulic cylinder to support oil pressures up to 480 bar and the use of heavy flywheels.

Acknowledgements

This work was performed within the Strategic Research Plan of the Centre for Marine Technology and Ocean Engineering, which is financed by Portuguese Foundation for Science and Technology (Fundação para a Ciência e Tecnologia-FCT) and the project “Generic hydraulic power take-off system for wave energy converters” funded by the Portuguese Foundation for Science and Technology (FCT) under contract PTDC/EMS-SIS-1145/2014. The testing has received support from MARINET, a European Community – Research Infrastructure Action under the FP7 “Capacities” Specific Programme, grant agreement nr. 262552. The research leading to these results is also part of the OceaNET project, which has received funding from the European Union’s Seventh Framework Programme for research, technological development and demonstration under grant agreement nr. 607656.

Appendix A. WEC Hydrodynamics

The WEC motion is determined with:

$$M_A = M_{FK} + M_D - M_R - M_{res} - M_{PTO} \qquad (25)$$

where M_A is the D’Alembert moment of inertia, M_{FK} is the moment due to undisturbed incident waves, M_D is the moment due to diffracted waves, M_R is the moment due to radiated waves, M_{res} is the hydrostatic restoring moment and M_{PTO} is the PTO control moment. The hydrodynamic radiation moment is determined with:

$$M_R(i\omega) = [B(\omega) + i\omega A(\omega)]\dot{\theta}(i\omega) = K_r(i\omega)\dot{\theta}(i\omega) \qquad (26)$$

where $B(\omega)$ and $A(\omega)$ are the frequency dependent hydrodynamic damping and added mass coefficients, respectively, and $K_r(i\omega)$ is the frequency response function of the radiation force. On the other hand the added mass and damping coefficients can be expressed with [13]:

$$A(\omega) = \lim_{\omega\to\infty} A(\omega) - \frac{1}{\omega}\int_0^\infty k(t)\sin(\omega\tau)d\tau \qquad (27)$$

$$B(\omega) = \int_0^\infty k(t)\cos(\omega\tau)d\tau \qquad (28)$$

Then Equation 25 is developed with Equations 26, 27 and 28, which gives:

$$(J+J^{\infty})\ddot{\theta}(t)+\int_{0}^{t}k(t-\tau)\dot{\theta}(t)+k_{res}\theta(t)+M_{PTO}(t)=M_{FK}(t)+M_{D}(t) \qquad (29)$$

The Equation 29 is computationally demanding because of the convolution term, but this convolution integral can be determined with [13]:

$$M_{ext}(t)=M_{FK}(t)+M_{D}(t)=\int_{-\infty}^{\infty}h_{e\eta}(t-\tau)\eta_{w}(\tau)d\tau \qquad (30)$$

Replacing Equation 30 in Equation 29 and without considering $M_{PTO}(t)$ gives:

$$(J+J^{\infty})\ddot{\theta}(t)+\int_{0}^{t}k(t-\tau)\dot{\theta}(t)+k_{res}\theta(t)=\int_{-\infty}^{\infty}h_{e\eta}(t-\tau)\eta_{w}(\tau)d\tau \qquad (31)$$

Appendix B.

The power of the electric drive is determined with:

$$P_{drive}=\frac{dW_{drive}}{dt}=P_{M}-P_{G}-P_{loss} \qquad (41)$$

where P_M is the motor power, P_G is the generator power, P_{loss} is the power loss in the electrical generator, assumed as constant. On the other hand the drive kinetic energy is given with:

$$W_{drive}=\frac{1}{2}I\Omega^{2} \qquad (42)$$

where Ω is the drive rotational speed.

On the other hand the drive torque is determined by taking the time derivative of Equation 41:

$$I\frac{d\Omega}{dt}=T_{M}-T_{G} \qquad (43)$$

The drive speed Ω is determined with a correction factor r applied on the drive speed at the model level Ω_m, when the maximum speed is above the one at the test rig, and then:

$$\Omega=\Omega_{G}=r\Omega_{m} \qquad (44)$$

where r is determined with:

$$r=\Omega_{G,nom}/\Omega_{17,m,nom} \qquad (45)$$

where $\Omega_{G,nom}$ is the nominal speed of the real generator and $\Omega_{17,m,nom}$ is the nominal speed of the generator model. Equation 45 is then developed with the Froude's scaling laws [13, 20, 34, 35]:

$$\Omega_{17,m}=\Omega_{17,p}\varepsilon^{-1/2} \qquad (46)$$

$$\Omega_{17,m,nom}=\Omega_{17,p,nom}\varepsilon^{-1/2} \qquad (47)$$

$$\varepsilon=(P_{17,m,nom}/P_{17,p,nom})^{2/7} \qquad (48)$$

The resulting equation is:

$$\Omega_G = \Omega_{G,nom}\Omega_{17,p}/\Omega_{17,p,nom} \qquad (49)$$

On the other hand, the torque sent to the real generator is corrected in order to compensate the correction made in the generator speed with Equation 49. This is carried out by replacing the time derivative of Equation 45 in Equation 43 and the resulting equation merged with:

$$I_m \frac{d\Omega_m}{dt} = T_{7,m} - T_{17,m} \qquad (50)$$

which gives:

$$T_M - T_G = r\frac{I}{I_m}(T_{7,m} - T_{17,m}) \qquad (51)$$

where I is the total moment of inertia of the electrical drive, r is the speed correction factor and I_m, $T_{7,m}$ and $T_{17,m}$ are the moment of inertia of the electric drive, four quadrant mode pump (7) and generator (17) torques at the model scale, respectively. The relations with the prototype are then made with the Froude's scaling laws [13, 20, 34, 35]:

$$I_m = \varepsilon^5 I_p \qquad (52)$$

$$T_m = \varepsilon^4 T_p \qquad (53)$$

where ε is the scale length and I_p, T_p and T_m are the moment of inertia of the prototype, prototype and model torques, respectively. Then, the inclusion of Equations 52 and 53 in Equation 51 results in:

$$T_M = r\varepsilon^{-1}\frac{I}{I_p}T_{7,p} \qquad (54)$$

$$T_G = r\varepsilon^{-1}\frac{I}{I_p}T_{17,p} \qquad (55)$$

Appendix C. Model parameters

Parameter	Symbol	Value	Unit
Accumulators			
Gravity acceleration	g	9.8	m/s^2
Ideal nitrogen constant	R	297	J/kg/K
Nitrogen specific heat ratio	c_v	743	J/kg/K
Nitrogen property	σ	129.5	---
Number of accumulators	n_6	7	---
Thermal time constant	τ	82.62	s
Thermal time constant 2	$\tau 2$	165.5	s
Size of accumulator	V_{g06}	50 x 10^{-3}	m^3
Wall temperature	T_w	323.15	K
Accumulator efficiency	η_{11}	0.95	
Actuators			
Annular area (Type I)	A_1	160.20	cm^2
Annular area (Type II)	A_1	100.53	cm^2
Number of actuators	---	1	---
Floater mechanism			
Arm, float and added inertia	J_{a+ad}	3.8 x 10^6	Kgm^2
Damping term	B	4.4 x 10^6	Mkgm^2/s
Distance A to C joints	l_2	3	m
Distance B to C joints	l_3	2.6	m
Distance A to B joints	l_4	1.6	m
Hydrostatic torque restoring coef.	k_r	14.1	Nm/rad
Inertia term	J	0	Kgm^2

Initial arm angle	α_0	62	deg
Spring constant	k	-6.7 x 10^6	Nm/rad
Flywheel material density	ρ	7830	kg/m^3
Generators			
Rated power of Generator 1		55	kW
Rated power of Generator 2		160	kW
Non-return valves			
Oil density	ρ_f	880	kg/m^3
Cracking pressure	Δ_{pcr}	0	Pa
Discharge coefficient	C_d	0.7	---
Number of valves per line	---	2	---
Orifice area	A_8	1.2 x 10^{-5}	m^2
Pipeline			
Fluid bulk modulus	β_{eff}	12 x 10^8	Pa
Fluid volume	V_{ext}	0	m^3
Pumps			
Maximum displacement	Vg_{7max}	250	cm^3/rot
	Vg_{10max}	250	cm^3/rot
	Vg_{12max1}	80	cm^3/rot
	Vg_{12max2}	250	cm^3/rot

References

[1] Falcão, AFO. Wave energy utilization: A review of the technologies. Renewable and Sustainable Energy Reviews 2010; 14 (3): 899-918. http://dx.doi.org/10.1016/j.rser.2009.11.003.

[2] Drew, B, Plummer, A, Sahinkaya, M. A review of wave energy converter technology. In: Proc IMechE Part A: J Power and Energy 2009; 223: 887-902. doi: 10.1243/09576509JPE782.

[3] Guedes Soares, C, Bhattacharjee, J, Tello, M, Pietra, L. Review and classification of wave energy converters. In: Marine Engineering and Technology, Guedes Soares, C., Garbatov, Y, Sutulo, S, Santos, T (Eds), Taylor and Francis Group. London, UK; 2012:585-594.

[4] Zhang, D, Li, W, Lin, Y, Bao, J. An overview of hydraulic systems in wave energy application in China. Renewable and Sustainable Energy Reviews 2012; 16 (7): 4522-4526. http://dx.doi.org/10.1016/j.rser.2012.04.005

[5] Falnes, J. Principles for Capture of Energy from Ocean Waves. Phase Control and Optimum Oscillation.In, Department of Physics, NTNU. Trondheim, Norway; 1995.

[6] Hansen, R, Kramer, M. Modelling and Control of the Wavestar Prototype. In: Proc 9th European Wave and Tidal Energy Conference (EWTEC 2011). Southampton, UK; 2011: pp 10.

[7] Salter, S, Taylor, J, Caldwell, N. Power conversion mechanisms for wave energy. In: Proc. Instn Engrs, Part M: J Engineering for the Maritime Environment 2002; 216:1-27.

[8] Vidal, E, Hansen, R, Kramer, M. Early Performance Assessment of the Electrical Output of Wavestar's prototype. In: Proc. 4th International Conference on Ocean Energy. Dublin, Ireland; 2012: pp 6.

[9] Henderson, R. Design, simulation, and testing of a novel hydraulic power take-off system for the Pelamis wave energy converter. Renewable Energy 2006; 31 (2): 271-283. http://dx.doi.org/10.1016/j.renene.2005.08.021

[10] Kordak, R. Hydrostatic Drives with Secondary Control: An Introduction Into the Drive Concept and System Characteristics, Rexroth, 2003.

[11] Hansen, R, Andersen, T, Pedersen, H. Model Based Design of Efficient Power Take-Off Systems For Wave Energy Converters. In: The Twelfth Scandinavian International Conference on Fluid Power. Tampere, Finland; 2011, 35-49.

[12] Hansen, R. Design and Control of the Power Take-Off System for a Wave Energy Converter with Multiple Absorbers. Alborg: Faculty of Engineering, Science and Medicine, Alborg University; 2013.

[13] Gaspar, J., Kamarlouei M., Sinha, A., Xu, H., Calvário, M., F.-X. Faÿ., Robles, E. Guedes Soares, C. Speed control of oi-hydraulic power take-off system for oscillating body type wave energy converters. Renewable Energy 2016; 97:769-783. http://dx.doi.org/10.1016/j.renene.2016.06.015.

[14] Gaspar, J., Calvário, M., Kamarlouei, M., Guedes Soares, C. Power Take-Off concept for wave energy converters based on oil-hydraulic transformer units. Renewable Energy 2016; 86:1232-1246. http://dx.doi.org/10.1016/j.renene.2015.09.035.

[15] Gaspar, J., Guedes Soares, C. Modelling pump efficiency in a generic hydraulic Power Take-Off for wave energy point absorbers. In: Maritime Technology and Engineering, Guedes Soares, C. and Santos, T (Eds), Taylor and Francis Group. London, UK; 2015: 1233-1241.

[16] Gaspar, J., Calvário, M., Guedes Soares, C. Pump and gas accumulator based phase control of wave energy converters. In: Renewable Energies Offshore, Guedes Soares (Ed.), Taylor and Francis Group, London, UK; 2015: 295-303.

[17] Penalba, M., Mérigaud, A., Gilloteaux, J. C., Ringwood, J.V. Nonlinear Froude-Krylov force modelling for two heaving wave energy point absorbers. In Proceedings of the 11th European Wave and Tidal Energy Conference, Nantes, France, 6-11 September 2015.

[18] Bacelli, G., Genest, R., Ringwood, J.V. Nonlinear control of flap-type wave energy converter with a non-ideal power take-off system. *Annu. Rev. Control* 2015, 40, 116-126.

[19] Penalba, M., Ringwood, J. V. A Review of Wave-to-Wire Models for Wave Energy Converters. Energies 2016; 9: 506; doi: 10.3390/en9070506.

[20] Henriques, J.C.C, Gomes, R.P.F, Gato, L.M.C., Falcão, A.F.O, Robles, E, Ceballos, S. Testing and control of a power take-off system for an oscillating-water-column wave energy converter. Renewable Energy 2016; 85:714-724.

[21] Henriques, J.C.C, Gato, L.M.C., Falcão, A.F.O, Robles, E, F.-X. Faÿ. Latching control of a floating oscillating-water-column wave energy converter. Renewable Energy 2016; 90:229-241. http://dx.doi.org/10.1016/j.renene.2015.12.065.

[22] Tecnalia Electrical PTO. URL http://www.tecnalia.com/en/energy-environment/infrastructure-a-equipment/infrastructure-a-equipment.htm). Last accessed date 2015.

[23] Hansen, R, Kramer, M, Vidal, E. Discrete Displacement Hydraulic Power Take-Off System for the Wavestar Wave Energy Converter. Energies 2013; 6:4001-4044. doi: 10.3390/en6084001.

[24] Pourmovahed, A, Otis, D. An experimental thermal time-constant correlation for hydraulic accumulators. J Dynamics Systems, Measurement and Control 1990; 112: 116-121.

[25] Sauer-Danfoss. Series 51-1 Bent Axis Variable Displacement Motors: Technical Information. 2009. URL http://files.danfoss.com/documents/520l0440.pdf. Last accessed date 2015.

[26] Jang, R.. ANFIS: Adaptive-Network-based Fuzzy Inference Systems, IEEE Transactions on Systems, Man, and Cybernetics, May 1993; 23 (3): 665-685.

[27] Mashrei, A. Neural Network and Adaptive Neuro-Fuzzy Inference System Applied to Civil Engineering Problems. INTECH Open Access Publisher 2012; 471-504.

[28] Zhibin, He, Xiaohu, Wen, Hu, Liu, Jun, Du. A comparative study of artificial neural network, adaptive neuro fuzzy inference system and support vector machine for forecasting river flow in the semiarid mountain region. Journal of Hydrology, Volume 509, 13 February 2014, Pages 379-386.

[29] ABB. Low voltage process performance motors according to EU MEPS. URL http://www.abb.pt/abblibrary/downloadcenter/. Last accessed data 2015.

[30] Eaton, Screw-in cartridge valves. URL http://www.eaton.com/ecm/groups/public/@pub/@eaton/@hyd/documents/content/pct_267525.pdf. Last accessed date 2014.

[31] Lee, C.H. & Newman, J.N. (2006). WAMIT User Manual, Versions 6.4, 6.4PC, 6.3S, 6.3 S-PC. WAMIT, Inc., Chestnut Hill, MA, USA.

[32] Liu, Z., Frigaard, P. (1997). Random seas. Aalborg University.

[33] Rexroth Bosch Group. Hydraulic cylinder mill type, Series CDH3/CGH3/CSH3. URL https://dc-us.resource.bosch.com/media/us/products_13/product_groups_1/industrial_hydraulics_5/pdfs_4/re17338.pdf. Last accessed date 2016.

[34] Vassalos, D. Physical modelling and similitude of marine structures. Ocean Engineering 1999; 26 (2): 111-123.

[35] Falcão, A.F.O, Henriques, J.C.C. Model-prototype similarity of oscillating-water-column wave energy converters. International Journal of Marine Energy 2014; 6: 18-34.

[36] Sinha, A., Karmakar, D., Guedes Soares, C. Numerical modelling of array of heaving point absorbers In: Renewable Energies Offshore, Guedes Soares (Ed.), Taylor and Francis Group, London, UK; 2015: 383-391.

[37] Fenner couplings. Section 5: Drive couplings. URL: http://www.fptgroup.com/dss/docs/708_05_Fenner_Couplings.pdf. Last accessed date 2016.

[38] Nexen. Clutch-brakes. URL: http://www.pneumax.co.th/Catalogue/PNE/Nexen-Clutch-Brake.PDF. Last accessed date 2016.

Analysis of electrical drive speed control limitations of a power take-off system for wave energy converters

José F. Gaspar[a], Mojtaba Kamarlouei[a], Ashank Sinha[a], Haitong Xu[a], Miguel Calvário[a], François-Xavier Faÿ[b], Eider Robles[b], C. Guedes Soares[a],*

[a] *Centre for Marine Technology and Ocean Engineering (CENTEC), Instituto Superior Técnico, Universidade de Lisboa, Av. Rovisco Pais, 1049-001 Portugal.*

[b] *TECNALIA. Energy and Environment Division, Parque Tecnológico de Bizkaia, 48160 Derio, Spain.*

*Corresponding author E-mail address: c.guedes.soares@centec.tecnico.ulisboa.pt

Highlights:

control approaches are simulated in a wave-to-wire model in a hardware in-the-loop simulation test rig

The model is based on a wave energy converter, being the wave, hydrodynamic and oil-hydraulic part simulated in a computer

Three different control strategies are developed and tested in this test rig

this drive is much more economical than an oil-hydraulic and equivalent one that is able to operate at those peaks of acceleration